



Toward Understanding the 3D Structure and Evolution of Magnetic Flux Ropes in an Extremely Long Duration Eruptive Flare

Zhenjun Zhou (周振军)^{1,2,3,4} , Jie Zhang⁴ , Yuming Wang^{1,3} , Rui Liu^{1,5} , and Georgios Chintzoglou⁶ 

¹ CAS Key Laboratory of Geospace Environment, Department of Geophysics and Planetary Sciences, University of Science and Technology of China, Hefei, Anhui 230026, China; zjzhou@mail.ustc.edu.cn

² School of Atmospheric Sciences, Sun Yat-sen University, Zhuhai, Guangdong, 519000, China

³ Synergetic Innovation Center of Quantum Information & Quantum Physics, University of Science and Technology of China, Hefei, Anhui 230026, China

⁴ Department of Physics and Astronomy, George Mason University, Fairfax, VA 22030, USA

⁵ Collaborative Innovation Center of Astronautical Science and Technology, China

⁶ University Corporation for Atmospheric Research (UCAR), Boulder, CO 80307, USA

Received 2016 December 13; revised 2017 November 5; accepted 2017 November 10; published 2017 December 20

Abstract

In this work, we analyze the initial eruptive process of an extremely long duration C7.7-class flare that occurred on 2011 June 21. The flare had a 2 hr long rise time in soft X-ray emission, which is much longer than the rise time of most solar flares, including both impulsive and gradual ones. Combining the facts that the flare occurred near the disk center as seen by the *Solar Dynamic Observatory* (SDO) but near the limb as seen by two *Solar Terrestrial Relations Observatory* (STEREO) spacecraft, we are able to track the evolution of the eruption in 3D in a rare slow-motion manner. The time sequence of the observed large-scale EUV hot channel structure in the Atmospheric Imaging Assembly (AIA) high-temperature passbands of 94 and 131 Å clearly shows the process of how the sigmoid structure prior to the eruption was transformed into a near-potential post-eruption loop arcade. We believe that the observed sigmoid represents the structure of a twisted magnetic flux rope (MFR), which has reached a height of about 60 Mm at the onset of the eruption. We argue that the onset of the flare precursor phase is likely triggered by the loss of the magnetohydrodynamic equilibrium of a preexisting MFR, which leads to the slow rise of the flux rope. The rising motion of the flux rope leads to the formation of a vertical current sheet underneath, triggering the fast magnetic reconnection that in turn leads to the main phase of the flare and fast acceleration of the flux rope.

Key words: Sun: coronal mass ejections (CMEs) – Sun: filaments, prominences – Sun: flares

Supporting material: animations

1. Introduction

The triggering mechanism and 3D coronal magnetic configuration during coronal mass ejection (CME) initiation are of great interest in solar physics; however, they are still under intense debate. The question remains as to whether or not the flux rope—a helical magnetic structure believed to lie at the heart of a CME—exists before the eruption (Qiu et al. 2007; Cheng et al. 2010; Zhang et al. 2012; Song et al. 2014; Liu et al. 2016). This is crucial to understanding the initiation mechanism of eruptions. White-light observations of CMEs in the outer corona often exhibit a typical “three-part” structure (Illing & Hundhausen 1985; Riley et al. 2008), consisting of a bright outer layer of compressed plasma followed by a large dark cavity and a bright prominence core in the cavity. A subset of interplanetary coronal mass ejections (ICMEs), the counterpart of CMEs observed in situ, contains so-called magnetic clouds (MCs), which can be well modeled as a large MFR based on the observed time sequence of the magnetic field (e.g., Burlaga et al. 1981; Gosling 1990; Lepping et al. 1990; Burlaga 1995; Kumar & Rust 1996; Vourlidis et al. 2013; Wang et al. 2015). These studies suggest that the fundamental magnetic structure of a CME is essentially an MFR, i.e., a structure of twisted magnetic field lines wrapping around a central axis.

However, the full 3D magnetic structure of CMEs prior to the eruption and during the early initiation phase remains elusive. A sigmoidal configuration in solar active regions prior to the eruption was often found in soft X-ray (SXR) and EUV

observations (e.g., Aurass et al. 1999; Canfield et al. 1999; Vrřnak et al. 2003; Canfield et al. 2007; Green & Kliem 2009; Tripathi et al. 2009; Green et al. 2010; Liu et al. 2010; Huang et al. 2011). These EUV and SXR sigmoids were often interpreted as the disk signature of MFRs (e.g., Pevtsov et al. 1996; Aurass et al. 1999; Canfield et al. 1999). Recently the EUV hot channels, i.e., observed in AIA 131 Å and 94 Å passbands, which correspond to a formation temperature higher than 6 MK, were found to continuously transform from a sigmoidal structure into a semicircular CME shape based on high-temperature passbands of the AIA instrument on board the *Solar Dynamic Observatory* (SDO), and the hot channel was interpreted as strong evidence of preexisting MFRs (Liu et al. 2010; Zhang et al. 2012). When seen along the axis of the hot channel, it appeared as a rising blob or “fire ball” of hot plasma (Cheng et al. 2011; Su & van Ballegooijen 2012; Patsourakos et al. 2013; Song et al. 2014). Patsourakos et al. (2013) presented the direct observational evidence of a fast CME being driven by a destabilized preexisting coronal MFR. Chintzoglou et al. (2015) uncovered the formation and preexistence of a flux rope via confined flaring events (8 hr before eruption) using AIA imaging that was also supported by nonlinear force-free field (NLFFF, e.g., Canou et al. 2009; Wiegmann & Sakurai 2012) extrapolations. Observational cases of preexisting flux ropes supported by modeling (in a similar way that modeling should be showing null points or hyperbolic flux tubes (HFTs) above active regions [ARs] as a support for the breakout scenario) are strongly suggesting that

flux ropes do preexist eruptions. All these studies inferred the existence of MFRs, which are intrinsically 3D in nature, from 2D projected imaging observations. However, the exact 3D structure of MFRs, such as the shape, height, and locations of footpoints, has not been directly measured and presented in these studies.

The exact pre-eruption magnetic structure should be intimately related to the triggering mechanism of CMEs, as elaborated by various theoretical models. Using the existence or nonexistence of MFRs as a discriminator, theoretical models largely fall into two different categories. The first category of models requires the preexistence of MFRs and argues that the ideal kink and/or torus MHD instability of MFRs triggers the eruption (Hood & Priest 1981; Kliem & Török 2006). The kink instability occurs if the twist, a measure of the winding of the field lines around the flux rope axis, exceeds a certain critical value (Hood & Priest 1981; Török et al. 2004; Kliem & Török 2006; Liu et al. 2016; Wang et al. 2016). The torus instability takes place when the overlying restraining magnetic field decreases fast enough that the restraining force could not balance the outward Lorentz self-force (or the hoop force due to the self-repulsion of the toroidal current) of the underlying arched MFR anymore; the onset of the instability can be characterized by a critical magnetic decay index along the height (Kliem & Török 2006; Olmedo & Zhang 2010). On the other hand, the second category of models does not require the preexistence of MFRs and assumes an alternative magnetic structure such as the sheared arcade. These models argue that the magnetic reconnection is the trigger of the eruption and also leads to the formation of a full MFR during the eruption (Antiochos et al. 1999; Moore et al. 2001).

The evolution process of CME eruptions, along with the associated flare, has distinct phases as shown from observations. Three distinct phases are conventionally defined based on the time profile of the *Geostationary Operational Environmental Satellites (GOES)* SXR emissions: preflare phase, rising phase, and decay phase. The impulsive phase of flares, a terminology adopted from hard X-ray observations (e.g., Benz 1993), is well known to correspond to the rising phase in SXR profiles. Previous studies revealed that the preflare and impulsive phases of a flare have a strong temporal correlation with the CME initiation and fast-acceleration phases, respectively (e.g., Zhang et al. 2001; Zhang & Dere 2006). Thus, the corresponding phases of flares and CMEs seem to be coupled and possibly controlled by the same eruption mechanisms. To describe these coupled stages, we use the nomenclature of (1) the precursor phase, (2) the impulsive phase, and (3) the decay phase. The precursor phase has been observed in flares across a wide electromagnetic spectrum, presenting emission enhancement before the impulsive phase in radio, H α , and UV to EUV multiwavelength spectroscopic observations (e.g., Bumba & Křivský 1959; Martin 1980; van Hoven & Hurford 1984; Cheng et al. 1985; Warren & Warshall 2001; Contarino et al. 2003; Fárník et al. 2003). Recently, Zhou et al. (2016) found a precursor signature acting as a transverse oscillation of the MFR prior to the onset of an X-class flare. Moore & Sterling (2006) have suggested that different initiation mechanisms may result in different precursor features. The precursor brightening that occurs near the magnetic polarity inversion line (PIL) fundamentally distinguishes the internal tether-cutting mechanism from the external tether-cutting (or breakout) mechanism. No precursor brightening has been predicted for the

eruption mechanism of the ideal MHD instabilities (Moore & Sterling 2006; Chifor et al. 2007).

The improved knowledge of the exact magnetic structure of CMEs, along with its evolution in the early stage, holds the key to understanding CMEs. In this paper, we address these important issues by analyzing the initial stage of a CME that erupted on 2011 June 21 with a speed of more than 700 km s⁻¹. In particular, this event has an unusually long rising phase in SXR, about 2 hr—the longest-rise-phase event to our knowledge. The evolution, in terms of morphology, temperature, and kinematics, all over a long time, presents us with the opportunity of a much more detailed study of CME initiation than most other events in the past. Further, the combined *SDO* and *Solar Terrestrial Relations Observatory (STEREO)* observations allow us to determine the exact 3D structure of the involved MFR before and during the eruption. Data and results are presented in Sections 2 and 3, respectively. We discuss the possible mechanisms to explain the observed evolution and make a summary in Section 4.

2. Instruments

The 3D morphology and evolution of the CME structure in the source region were observed from low to high temperatures in multiple wavelengths and from different viewing angles in space. On 2011 June 11, *STEREO* Ahead and Behind were about 94° west and 92° east, respectively from the Sun–Earth line along the ecliptic orbit around the Sun, while the *SDO* was situated near Earth. The AIA (Lemen et al. 2012) on board the *SDO* (Pesnell et al. 2012) and the Extreme Ultraviolet Imaging Telescope (EUVI; Wuelser et al. 2004) of the SECCHI instrument suite (Howard et al. 2008) on board the two *STEREO* spacecraft respectively observe the whole disk of the Sun in the range of 1–1.3 R_{\odot} and 1–1.6 R_{\odot} . We use the EUV images of AIA in the following specific passbands (with the primary emission ions and formation temperatures in AR and flare conditions; O’Dwyer et al. 2010): 171 Å (Fe IX at $T \sim 0.63$ MK), 193 Å (Fe XII/Fe XXIV, $T \sim 1.6$ and 20 MK), 211 Å (Fe XIV at $T \sim 2$ MK), 335 Å (Fe XVI at $T \sim 2.5$ MK), 94 Å (Fe XVIII at $T \sim 6.3$ MK), and 131 Å (Fe VIII/XXI/XXIII, $T \sim 0.4, 11,$ and 16 MK), with the remaining passband, 304 Å dominated by He II, formed at $T \sim 0.05$ MK, respectively (AIA; Boerner et al. 2012; Lemen et al. 2012). The same passband of 304 Å from both the *STEREO-A/B-EUVI* suits is used to ensure the same low-temperature structure seen from different views in space, thus allowing the 3D reconstruction of the structure of concern. The X-ray Telescope (XRT; Golub et al. 2007) on board *Hinode* (Kosugi et al. 2007) provides coronal images in a broad temperature range (~ 1 –10 MK; Narukage et al. 2011). Meanwhile, the AIA hot passbands (~ 10 MK at 131 Å and ~ 6.4 MK at 94 Å) would also provide observations of the hot structure with much higher temporal and spatial resolutions. Note that the AIA 131 Å passband contains both hot (10 MK) and cool (0.4 MK) components. *RHESSI* (Lin et al. 2002) provides images of solar flares in energetic photons allowing spectrum analysis of both thermal and nonthermal emissions. *GOES* SXR records the SXR flux ranging in separate passbands, 1.0–8.0 Å and 0.5–4.0 Å. Combining the observations from all these instruments, the low-temperature filament, warm coronal loops, and hot eruptive features were all sufficiently distinguishable.

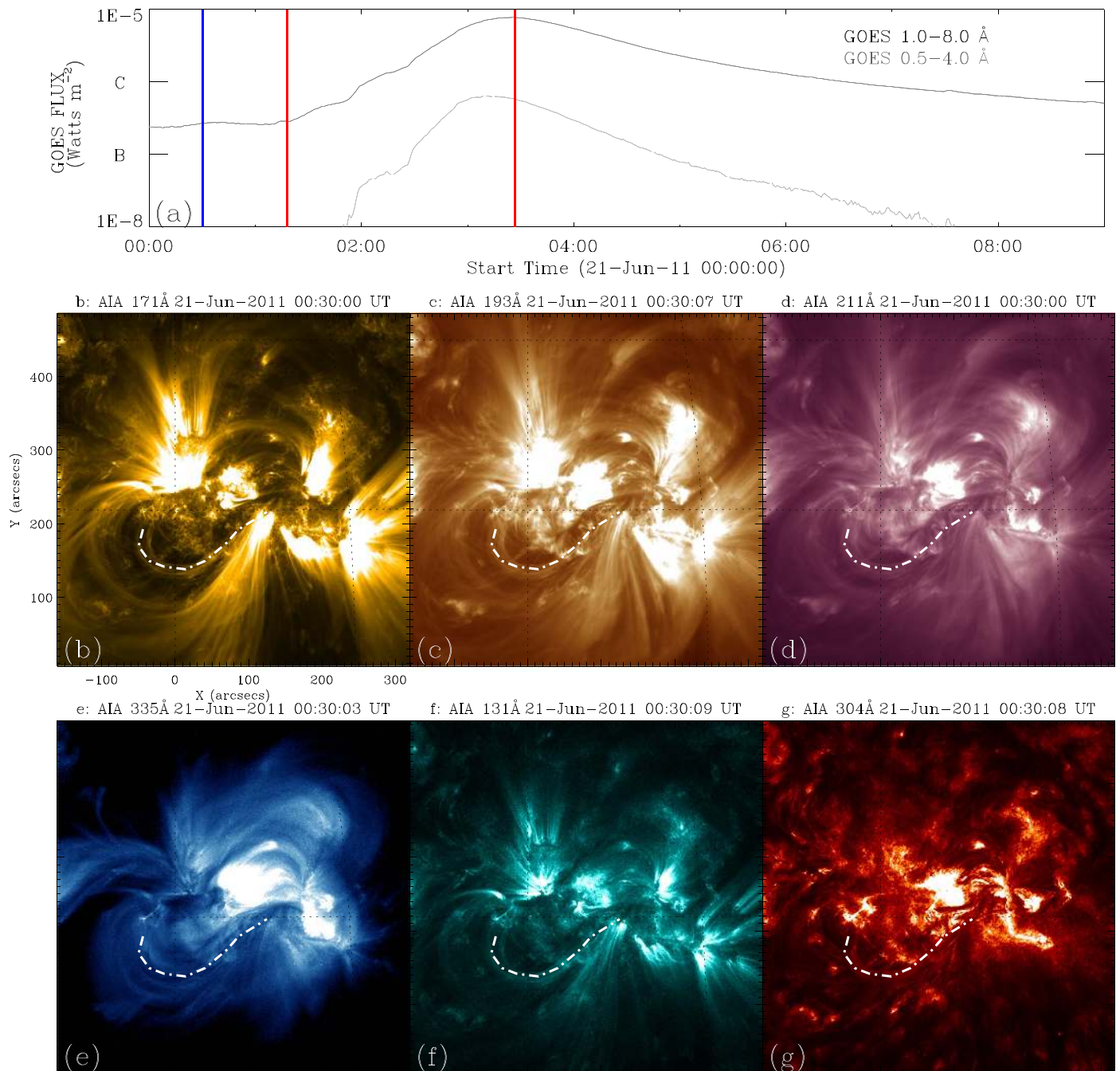


Figure 1. Overview of the 2011 June 21 long-duration flare. (a) *GOES* SXR integrated flux profiles in the range of 1.0–8.0 Å and 0.5–4.0 Å, respectively. The 1.0–8.0 Å flare onset time (01:18 UT) and peak time (03:26 UT) are marked with red lines. The vertical blue line indicates a preflare time at which the *SDO/AIA* took the images showing below (b) 171 Å (~0.63 MK), (c) 193 Å (~1.6 and 20 MK), (d) 211 Å (~2 MK), (e) 335 Å (~2.5 MK), (f) 131 Å (~0.4 and 10 MK), and (g) 304 Å (~0.05 MK). In all these images, part of the sigmoidal structure has been shown with a white dotted-dashed line near the center of the fields of view.

3. Observations and Results

3.1. The Event

On 2011 June 21, a *GOES* C7.7-class SXR flare occurred with the onset time at 01:18 UT, based on the SWPC (Space Weather Prediction Center) report. The unusual property of this event is that its 1.0–8.0 Å SXR flux gradually increased for more than 2 hr and finally reached its maximum value at 03:26 UT; the SXR flux returned to the pre-eruption background level at around 12:00 UT, about 8 hr later. Obviously, this is an extremely long duration event (LDE). The entire event lasted as

long as 11 hr (Figure 1(a)). The rising phase for most flares usually lasts for minutes or tens of minutes (Sterling & Moore 2005; Williams et al. 2005; Schrijver et al. 2008), but no more than 1 hr. The 2 hr long rising phase of this event is rare, indicating that the event had experienced an unusually slow change with time during its energy release phase when the flare flux was increasing and CME acceleration was ongoing. This property of slow initiation is an obvious advantage for the research of the initiation mechanism of solar eruptions, since detailed evolution could be obtained from prolonged observations.

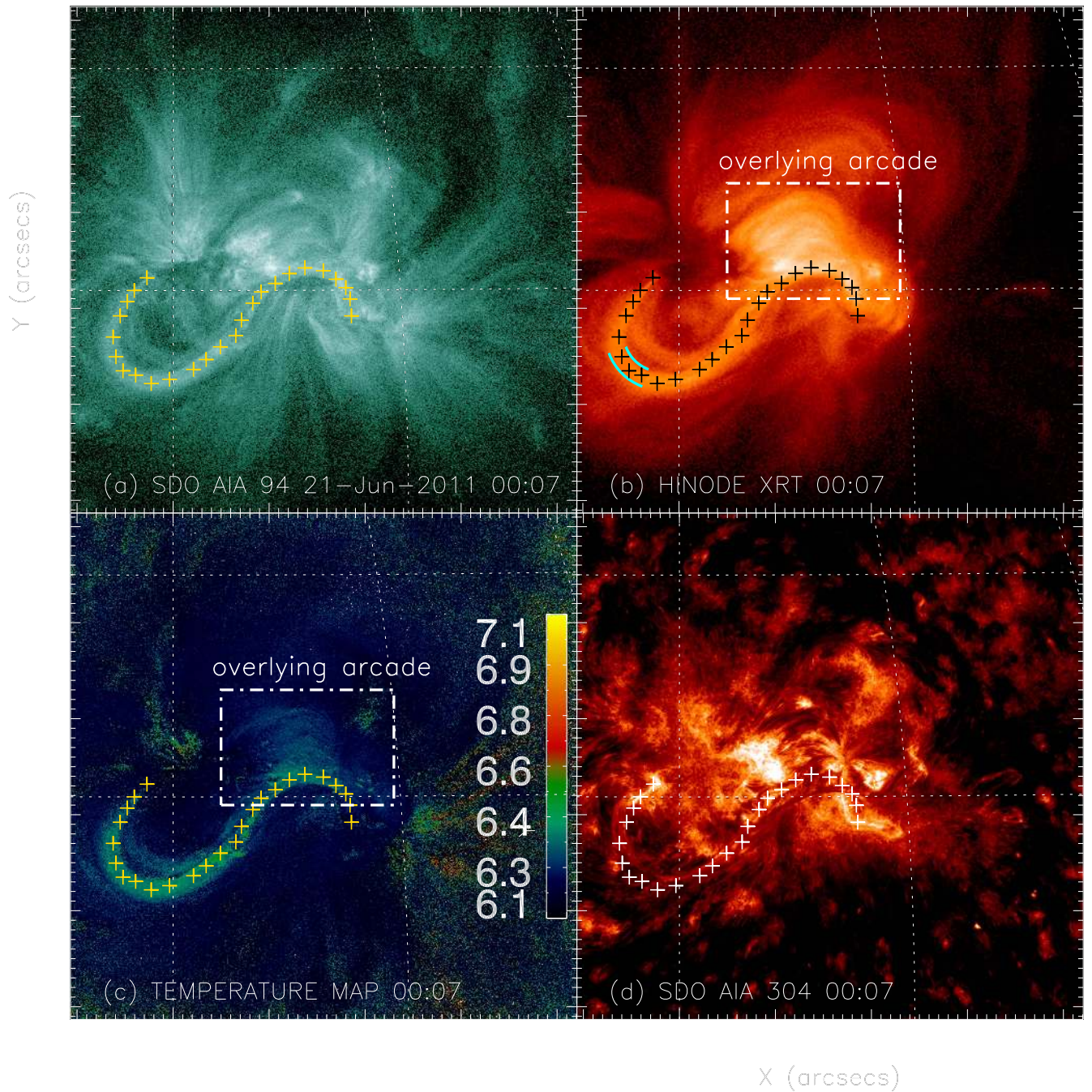


Figure 2. Pre-eruption sigmoidal structure seen as an EUV hot channel in (a) the *SDO/AIA* 94 Å passband and (b) *Hinode/XRT* SXR. The sequence of the crosses represents the path of the sigmoid. The map of DEM-weighted average temperature (panel (c)) gives a similar morphology to the sigmoid. Along the path of the sigmoid, a filament shares the same location (panel (d)). The dotted box marks out the area of the overlying arcades (panels (b) and (c)). The green arcs marked on the east elbow in panel (b) show the apparent width.

The pre-eruption structures in various temperatures of this long-duration event are shown in Figures 1 and 2. The source region is located in NOAA AR 11236 at coordinates of $\sim 16^\circ$ east, 04° north as seen from Earth during the period of the event. A distinct J-shaped structure resided in the AIA images of low-temperature passbands (Figures 1(b)–(d)), and it became slightly more diffusive in the AIA warm passband at 335 Å (Figure 1(e)). In the AIA 131 Å hot passband (Figure 1(f)), a bright J-shaped structure was present and shared the same position as the filament observed by the AIA 304 Å passband (Figure 1(g)). Due to the blending emission from the cool ~ 0.4

MK Fe VIII line at 131 Å, the hot component is not easily distinguished from the cool component, such as coronal loops and filaments, as the source active region is close to the disk center. To further investigate the hot component that may isolate the potential erupting structure in the core region, the six AIA optically thin coronal passbands, i.e., 131 Å, 94 Å, 335 Å, 211 Å, 193 Å, and 171 Å, are used to reconstruct the map of differential emission measure (DEM) weighted average temperature based on the DEM methods (Schmelz et al. 2011; Cheng et al. 2012; Hannah & Kontar 2012; Song et al. 2014). The observed flux F_i is the result of the convolution of the

emission with the instrument response., i.e.,

$$F_i = \int R_i(T) \times \text{DEM}(T) dT, \quad (1)$$

where $R_i(T)$ is the temperature response function of filter i . For this work, the “xrt dem iterative2.pro” (Golub et al. 2004; Weber et al. 2004) routine in the Solar SoftWare (SSW) package (<http://www.lmlsal.com/solarsoft>) is utilized to compute the DEM. In this procedure, the initial DEM is guessed and folded through the $R_i(T)$ to generate predicted fluxes, which are iteratively used to reduce the χ^2 between the actual and “model” observations. Further details and testing of the robustness of the method were discussed by Cheng et al. (2012). In this paper we use a parameter that characterizes the overall temperature of the plasma, i.e., the DEM-weighted average temperature per pixel defined in the following formula:

$$\bar{T} = \frac{\int \text{DEM}(T) \times T dT}{\int \text{DEM}(T) dT}. \quad (2)$$

After pixel-by-pixel calculation, a map of DEM-weighted average temperature (Song et al. 2014) has been reconstructed as shown in Figure 2(c). A conspicuous high-temperature sigmoidal structure is now standing out in the same active region; such a sigmoid appeared about 1 hr prior to the onset of the flare. This structure is also recorded in the sigmoid catalog: aia.cfa.harvard.edu/sigmoid.shtml (Savcheva et al. 2014). From the Earth view, a branch of filament is projected onto the same site where the hot sigmoid is located (Figure 2(d)). These observations indicate that the sigmoidal structure is about 6 MK hot, while also containing a significant amount of cool filament material along the same PIL. This kind of multi-temperature component sigmoidal structure has been considered as good evidence of an MFR existing before the onset of the precursor phase. Furthermore, there existed a high-temperature arcade surrounding the hook section on the west part of the sigmoid. These overlying arcades can be seen from the XRT image (Figure 2(b)) and the map of DEM-weighted average temperature (Figure 2(c)). The presence of the arcade on the west obscured the full view of the sigmoid in the west, thus making the whole structure appear more like a J shape in the XRT image owing to its broad temperature coverage.

3.2. 3D Reconstruction of the Sigmoid

Sigmoidal regions are more likely to erupt than nonsigmoidal regions. By analyzing 117 active regions observed by *Yohkoh* SXT in 1993 and 1997, Canfield et al. (1999) found that 84% of sigmoidal regions were eruptive, whereas 50% of nonsigmoidal regions were eruptive. Yet, its exact 3D structure has not been obtained in almost all previous studies. There is no doubt that an observed sigmoid should be intimately related to the configuration of a perceived MFR, from which a CME originates. However, because of the lack of direct measurement of magnetic fields in the corona, there remains a controversy on how exactly a sigmoid is related to an MFR. One theory argued that the sigmoid shows the emission of the main body of a kinked flux rope (Rust & Kumar 1996); on the other hand, in the popular model of Titov & Démoulin (1999), the sigmoid is the boundary layer of a largely unkinked flux rope, or the so-called bald patch separatrix surface. Here we simply show that

the observed sigmoidal structure is the structure of the MFR itself.

A sigmoid is usually traced out by emissions from hot plasmas, as illustrated in Figures 2(a)–(c). On the other hand, it could also be traced out by the existence of a filament, as shown in Figure 2(d), when the cool material of the filament and the hot material of the sigmoid, both located within or close to the flux rope, are nearly co-spatial. It is generally regarded that the cool filament material is collected at the dips of helical field lines in an MFR and is supported by the tension force of the magnetic field lines against the gravity (Gibson & Fan 2006, and references therein). Model calculations show that there exists a close spatial association between the total distribution of the extrapolated MFR dips and the whole filaments (Pevtsov et al. 2002; Guo et al. 2010; Tandberg-Hanssen 2013). Cheng et al. (2014b) showed that the hot EUV channel, the EUV counterpart of usually X-ray sigmoids, overlapped well with the prominence for an eruption over the limb. Thus, we believe that, for the event of study in this paper, the observed filament structure traces out the sigmoid and also the presumed MFR.

Using filament/prominence observations from multiple spacecraft, we employ the method of tie pointing (SCC MEASURE) within the *STEREO* branch of the Solar SoftWare (SSW) package (<http://www.lmlsal.com/solarsoft>), to reconstruct the exact 3D structure of the observed sigmoid. The tie-pointing method is based on the exact identification of the same point in 3D space as viewed from different angles (Thompson 2009). As shown in Figure 3, *SDO* was placed into an inclined geosynchronous orbit around Earth. *STEREO-A* is located approximately perpendicular ($\angle A \odot S = 92^\circ$) from the Sun–Earth line in a heliocentric orbit ahead of Earth; a similar angle exists between *STEREO-B* and *SDO* ($\angle B \odot S = 94^\circ$), but on the other side of the orbit. When one point (X_1, Y_1) is selected on a feature in the image from one viewing angle, for example, as with the blue point shown in Figure 3(c) (*SDO*), the procedure then calculates a line in 3D space corresponding to the line connecting the selected feature and the *SDO* and then projects the line onto the images from other viewing angles, e.g., Figures 3(b) (*STEREO-B*) and (d) (*STEREO-A*). The point (X_2, Y_2) at the intersection between the projected line and the identified feature, as indicated by the blue arrow in Figure 3(d), in combination with the original point (X_1, Y_1), can be used to calculate the true 3D coordinates (X, Y, Z) of the selected point, based on 3D triangulation. In order to avoid any false identification of common features of images from different viewing angles, the time-elapse evolution of features has been carefully examined to ensure the consistency. Images from the same passband (304 Å wavelength) are used to guarantee the observation of the same feature from different views, which may vary significantly from cool to hot temperatures. Also note that filaments are usually optically thick in 304 Å wavelength; thus, the line-of-sight integration effect is of no concern. However, due to possible occultation of multiple optically thick components along the line of sight, both images from *STEREO-A* and *STEREO-B* were used to help resolve the occultation effect, revealing the front and rear parts (corresponding to western and eastern parts from *SDO*; see Figure 3) along the filament. With these procedures, the 3D heliocentric inertial coordinates (HICs) of any commonly identified features are determined.

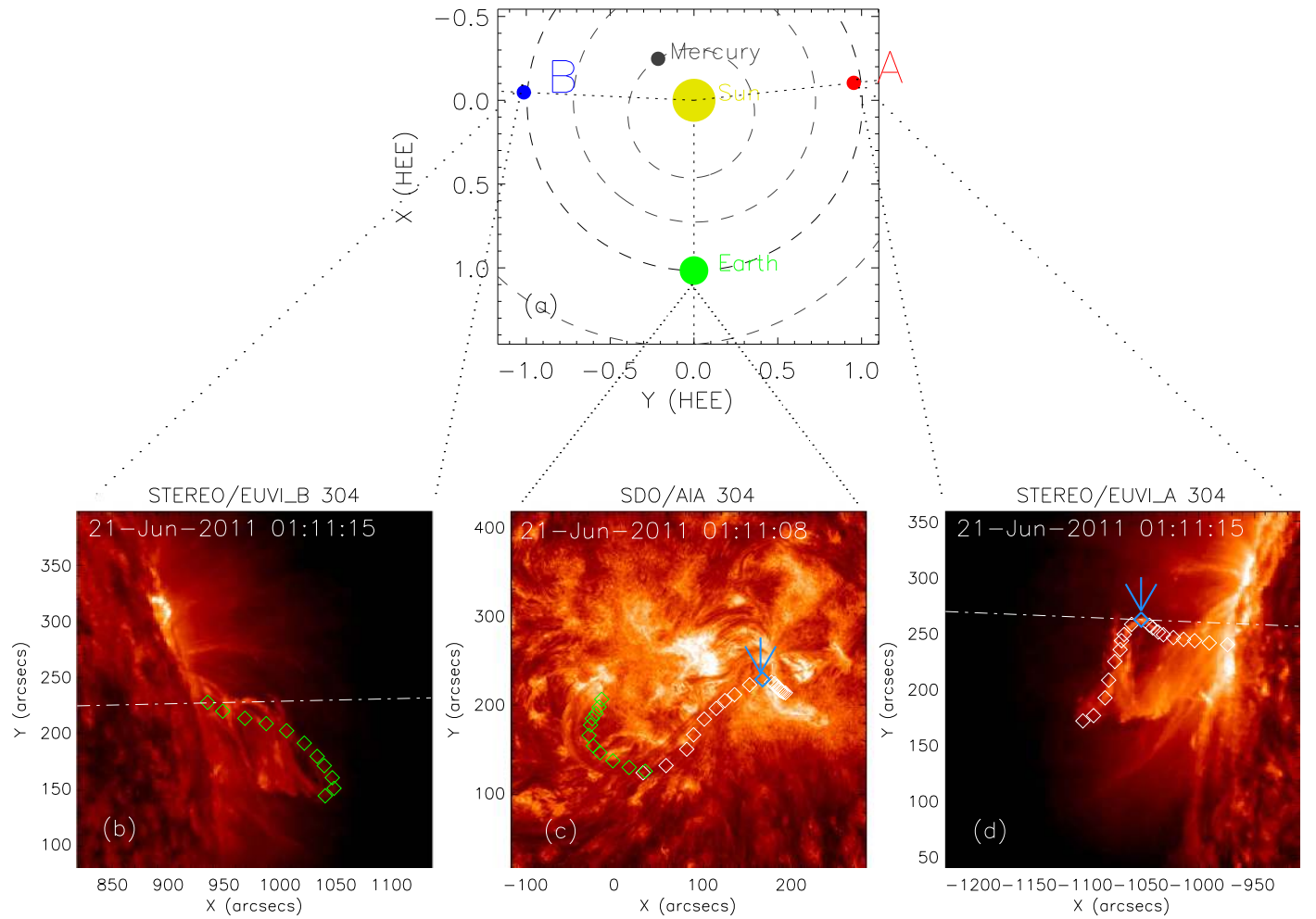


Figure 3. Illustration of the tie-pointing method for 3D reconstruction. (a) Three satellites’ positions in the heliocentric Earth ecliptic coordinate system: *SDO* is fixed at the L1 point—the front view for the filament; *STEREO-A* and *STEREO-B* sit along the direction of the opposite end sides of the filament. The separation angles between *SDO* and *STEREO-A/B* are nearly perpendicular, -92° and 94° , respectively. Panels (b)–(d) show the filament in three different viewing angles. The diamond symbols show the corresponding projected filament structure. To avoid the obscuring effect, the western part of the filament is reconstructed utilizing the *SDO* and *STEREO-A*, while the eastern part is reconstructed utilizing the *SDO* and *STEREO-B*. The point denoted by an arrow in the *SDO* image (panel (c)) corresponds to the blue point along the line of sight in the *STEREO-A* image (panel (d)).

Based on the method described above, we have determined the exact 3D coordinates of many points along the filament. Due to the tight coupling between filament and flux rope, from observations we can now finally determine the true 3D skeleton of the MFR, as shown in Figure 4, which is arranged from left to right with different parts as eastern footpoint, upper-ward eastern leg, curved eastern elbow, horizontal arm and shoulder, western elbow, western leg, and western footpoint. Although we can exactly determine the topology of the MFR along the main axis, we could not accurately measure the size of the cross section perpendicular to the main axis. It is accepted that a solar filament only fills the lower volumes of the flux rope (Rust & Kumar 1994; Chae et al. 2001; Guo et al. 2010). Here we assume that the cross-sectional size shall be larger than that of the observed filament and set the size at 0.02 solar radius to coincide with the east elbow’s apparent width measured from the *Hinode* XRT image (Figure 2(b)). Note that this is not a well-constrained physical value and is mainly adopted for the purpose of visualization. The 3D model of the MFR in Figure 4 is shown against the true surface obtained from the synoptic magnetogram map from HMI line-of-sight observations. The PARAVIEW software package, a 3D tool used for interactive

scientific visualization (for more details, see <http://www.paraview.org>), is used to render the model.

While the MFR in this event appears as a sigmoid or “S” shape on the projected solar disk as observed from the top, its overall topology in 3D can be described as an “m” shape with the middle leg missing as shown in Figure 4(d): the western leg sharply rises up to its western elbow from the solar surface with an elevation angle of about 69° and then slowly stretches toward the east along the elbow. The arm and shoulder part, represented by the horizontal line at the top, runs high in the corona and nearly in parallel with the surface but has a shallow dip in the middle. On the east, the flux rope quickly drops down from the eastern elbow to the eastern leg, which intersects the surface with an elevation of about 54° . The average height of the main body (i.e., the arm and shoulder part) is about 60 Mm. The property of high-lying and large size of the MFR may help explain the extremely long duration property of the event.

From Figure 4, one can easily identify the projection effect on the appearance of the MFR. It appears as a sigmoid as seen from *SDO*, or the top view (Figure 4(c)). On the other hand, it appears as the shape “8” as viewed from *STEREO-B*, or the side view from the east (Figure 4(b)). From all these

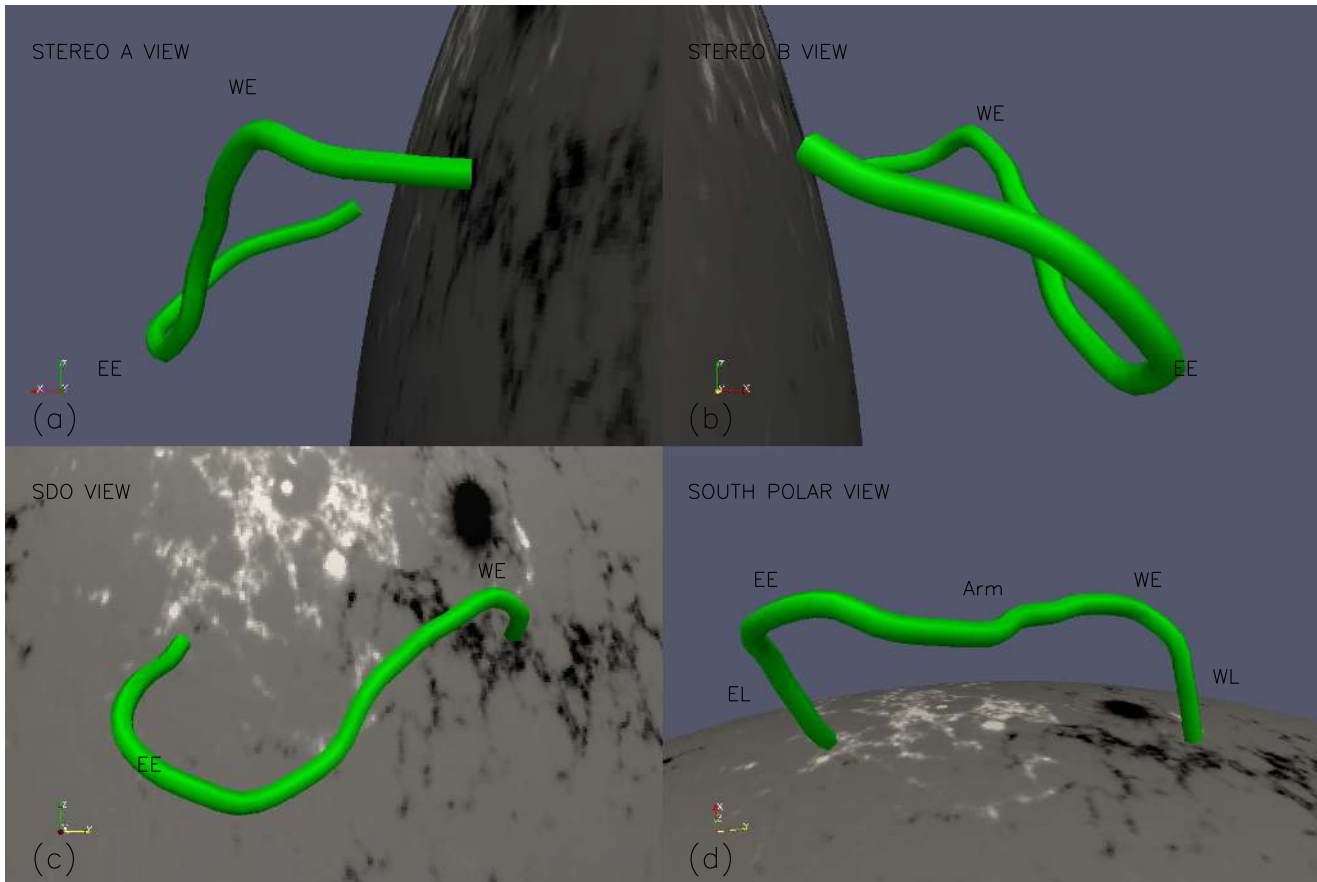


Figure 4. 3D structure of the reconstructed filament or MFR shown from different viewing angles. An “8” shape in panels (a) and (b) is captured by the *STEREO*/EUVI-A and EUVI-B, but it is more like an “S” shape in panel (c), in the view of *SDO*/AIA. An “m” shape is shown in panel (d) from the south pole view. The marks of “WE” (western elbow, the curved part) and “EE” (eastern elbow, the curved part) are at the same location in 3D in all these panels. “EL” shown in panel (d) means the east leg part, “WL” means the west leg part, and the middle horizontal section is the arm and shoulder part.

(An animation of this figure is available.)

perspectives, we now understand why this MFR had a sigmoidal shape as projected onto the solar disk: the western elbow was slightly kinked or writhed toward the north, while the eastern elbow along the arm part was significantly kinked toward the south; the main orientation of the flux rope, determined by the locations of the two footprints, was nearly along the east–west orientation. From the top view, it was more like a “J” shape than an “S” shape, because one of the elbows has little horizontal component projected onto the solar disk to form a hook shape. We further note that there is an asymmetry in the shape, i.e., the eastern elbow is higher than the western elbow.

3.3. Kinematic Evolution

To find out the kinematic evolution of the event, we track certain features that can be consistently observed over the time during the early dynamic evolution. The distance–time plot for the prominence observed by *STEREO-B* 304 Å in a slice along the eruption direction is shown in Figures 5(a) and (b). The solar rotation has little effect on the variation of the prominence height during the period of the study. The angular velocity of the Sun at the latitude of AR 11236 is $0^{\circ}61$ per hour. During the entire 11 hr period of the flare, the Sun rotated less than 7° , which corresponds to a change of height of ~ 0.5 Mm at a height of 60 Mm. The lower panel shows the distance–time plot of the hot plasma in a slice along the direction of the

movement of the eastern elbow of the hot sigmoid (Figures 5(c) and (d)). The filament and sigmoid movement trajectories are marked by red triangles in Figures 5(b) and (d), top panels. Only some of the selected points are plotted on the diagram to display the trajectories, to avoid shading the features behind. The derived velocity–time plots of the two features are shown in Figures 5(b) and (d), bottom panels. Here we assume that the uncertainty of the height of the selected feature points is 5 pixels. The associated uncertainty of the derived velocity is indicated by the shadings.

There existed two distinct phases during the eruption as seen from the kinematic changes and *GOES* X-ray profile: a precursor phase from 01:30 UT to 02:20 UT and an impulsive phase (or main phase) starting from 02:20 UT until possibly the peak time of the flare. The two phases are most clearly separated around 02:20 UT as indicated by the vertical red dot-dashed line, but more accurately by a jump in X-ray emission 7 minutes later in *GOES* high channel in $0.5\text{--}4.0$ Å, denoted by a red arrow in Figure 5(b). Prior to 01:30 UT, both the prominence in cool temperature and the sigmoid in hot temperature kept nearly stable, or experienced an unnoticeable rising at best. After about 01:30 UT, the prominence started to slowly rise up at a speed on the order of 10 km s^{-1} (Figures 5(b) and (d), bottom panel). After $\sim 01:50$ UT, the filament experienced a slow acceleration and made it speed up to 50 km s^{-1} ; after 02:10 UT, this feature obtained a speed of

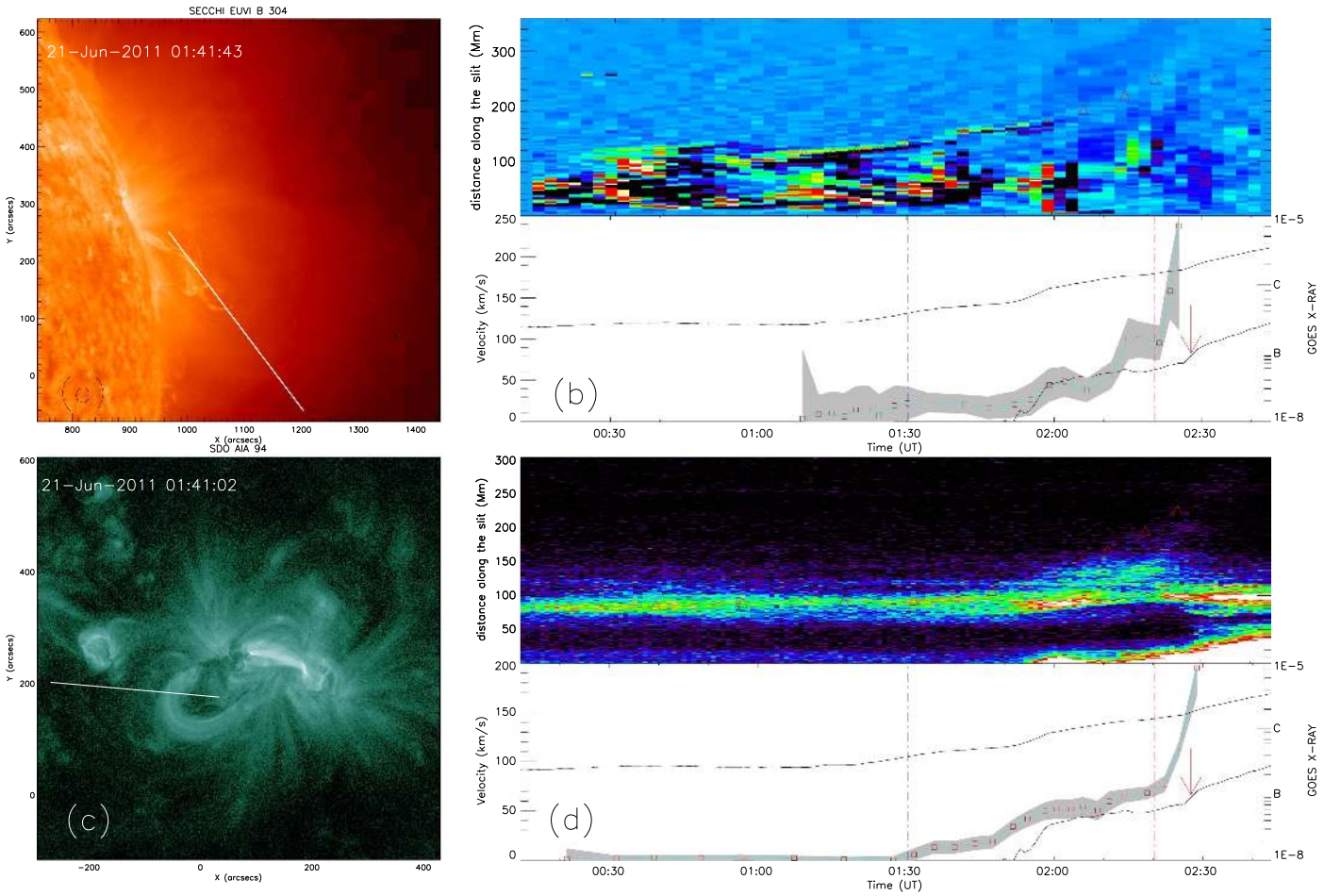


Figure 5. Kinematic evolution of the eruption. The selected slice used for creating distance–time plots is shown in panel (a) for *STEREO*/EUVI-B 304 Å (~ 0.05 MK) and panel (c) for *SDO*/AIA 94 Å (~ 6.3 MK). In the first row of panel (b) (or panel (d)), the red triangle symbols depicts the front evolution of the filament (or the hot channel). In the second row, the derived velocity of the filament (or the hot channel) is shown along the profiles of *GOES* SXR fluxes. The associated uncertainty of the derived velocity is indicated by the shading. The vertical blue line indicates the onset of the flare precursor phase, and the vertical red line marks the onset of the impulsive phase. A red arrow points out the sudden radiation flux enhancement in the *GOES* SXR high channel.

more than 200 km s^{-1} . This particular feature could not be easily further traced out owing to the quick depletion of the prominence material when it reached high corona. Since the prominence was observed above the limb, the velocity obtained should have a minimal projection effect. On the other hand, the related hot sigmoid viewed from the *SDO*/AIA 94 Å (6.3 MK) had a similar kinematic behavior, though its derived velocity was subject to a severe projection effect (Figures 5(c) and (d)). The sigmoid appeared stationary before 01:30 UT. The velocity had a small increase up to 20 km s^{-1} between 01:30 UT and 01:50 UT. From 01:50 UT, we can see that the sigmoid had a small but obvious acceleration, with the speed changing from 20 to 50 km s^{-1} . Emission of the *GOES* high passband (0.5–4.0 Å) simultaneously increased by almost one order of magnitude. The second phase, the so-called impulsive phase, began at about 02:20 UT. The structure became fully unstable and eruptive: the front velocity of the sigmoid presented a strong acceleration after 02:20 UT, denoting the onset of the fast eruption of the CME. This phase is well known as the CME acceleration phase (Zhang et al. 2001). The evolution of the erupted MFR front is approximated by a two-stage model consisting of a preceding linear stage and a following exponential stage in velocity (Cheng et al. 2014a, and references therein).

3.4. X-Ray Spectrum Analysis

Accompanied by the kinematic evolution of the filament and the sigmoid structure, the energetic emission feature in X-rays with *RHESSI* also revealed an interesting evolution pattern. For this analysis, we focus on times during the precursor phase and the impulsive phase. In order to ensure a reliable data set of *RHESSI*, a careful selection is taken to avoid the effort of attenuator state changes, satellite night times, South Atlantic Anomaly (SAA), and other complexities like photon pileup and decimation of data due to instrumental overflow. Figure 6 (and the accompanying movie) shows the reconstructed X-ray sources of the event from *RHESSI* observations, which are overlapped on the *SDO*/AIA 94 Å images. Before 02:20 UT, or during the precursor phase, the X-ray source region is only located near the western elbow of the sigmoid with a relatively low energy range (3–6, 6–12 keV); a 12–25 keV or higher hard X-ray source could not be constructed during this period. After 02:20 UT, or during the impulsive phase, the main X-ray emission sources had changed to the middle of the arm/shoulder part of the sigmoid. The higher-energy channel 12–25 keV became visible in the impulsive phase. We fit the X-ray spectrum with the Object Spectral Executive (OSPEX) software package for source regions in both the precursor phase and impulsive phase (Figure 7). Its spatially integrated,

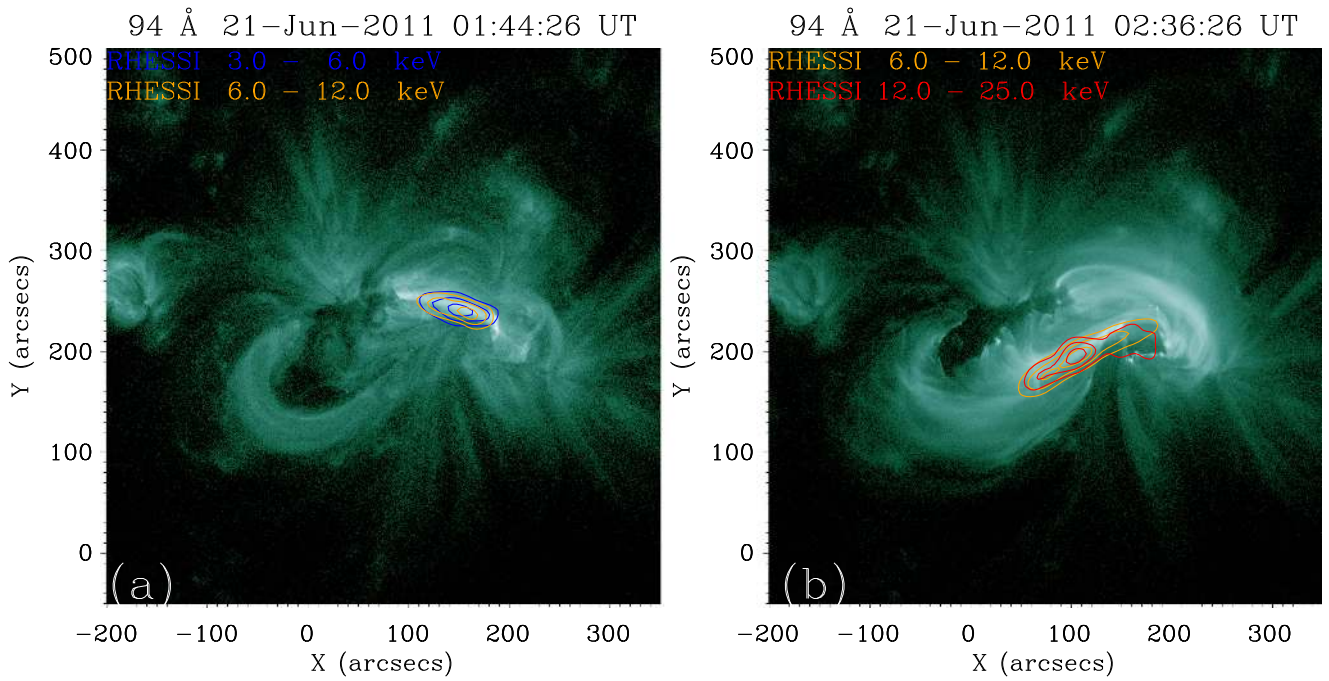


Figure 6. AIA 94 Å images (background) with *RHESSI* contours during the (a) precursor and (b) impulsive phases. The overlaid contours are from *RHESSI* X-rays; the blue, orange, and red contours correspond to 3–6 keV, 6–12 keV, and 12–25 keV, respectively. The levels are set at 50%, 70%, and 90% of the maximum brightness accumulated by detectors 4–8.

(An animation of this figure is available.)

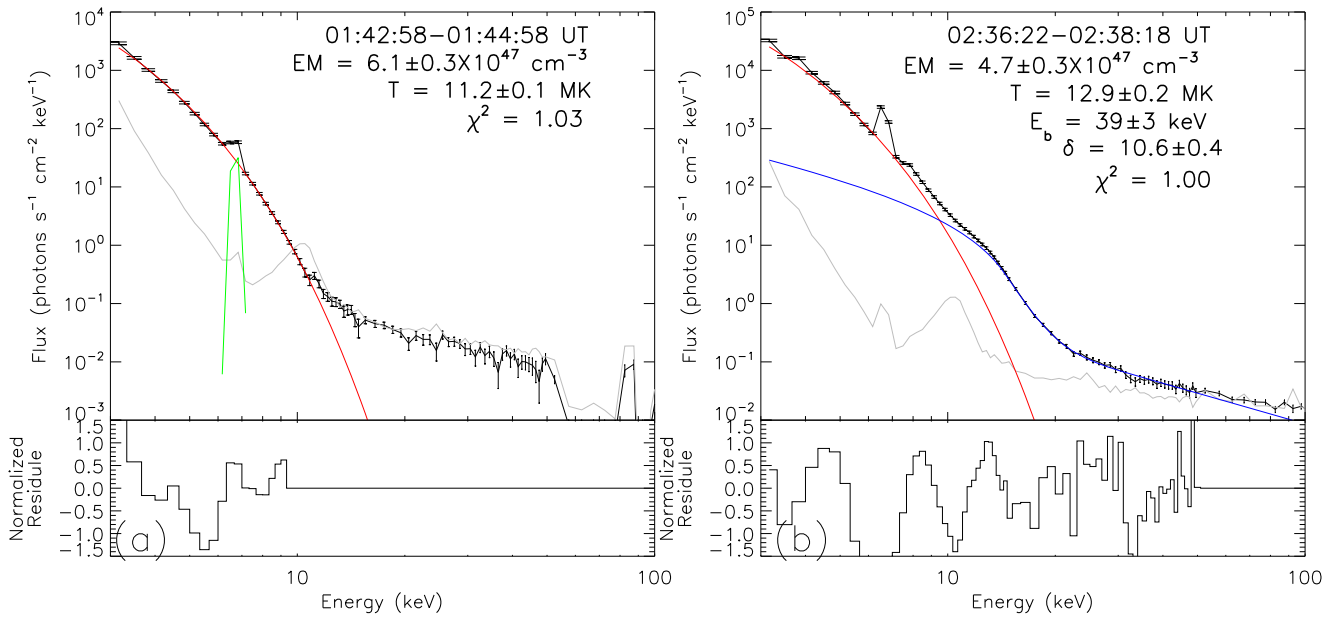


Figure 7. *RHESSI* flare source spectral profiles with the corresponding spectral fits. Panels (a) and (b) illustrate *RHESSI* spatially integrated, background-subtracted spectra and the corresponding spectral fits during time intervals corresponding to Figures 6(a) and (b), respectively. The red line indicates an optically thin thermal bremsstrahlung radiation function, the blue line a thick-target bremsstrahlung version-2 model (thick2), the green line a Gaussian function, and the gray line the background. The fitting parameters are marked in each panel, including emission measure (EM), temperature (T), break energy in the electron distribution function (E_b), power-law index (δ) of the electron distribution function below the break energy, and chi-square (χ^2) of each fitting, assuming a system uncertainty of 5%. Fitting residuals normalized to the 1σ uncertainty of the measured flux are shown at the bottom. Detectors 1, 3, 4, 5, 6, 8, and 9 are used.

background-subtracted photon flux is fitted by a variable thermal component (Vth) for the optically thin thermal bremsstrahlung radiation and thick-target bremsstrahlung spectrum from an isotropic electron distribution Version-2 model (thick2) for the nonthermal photon flux that is due to the interaction of energetic electrons with thick-target plasma. The result shows that the source region at the western elbow during

the precursor phase mainly behaved as a single thermal source with a fitted temperature of 11.2 MK. On the other hand, the source region that appeared at the arm part after 02:20 UT had the nonthermal contribution dominating over the thermal component at energies above ~ 10 keV; the spectral index for the thick-target bremsstrahlung is 10.6 with an uncertainty of 0.4. This analysis revealed the corresponding X-ray radiation

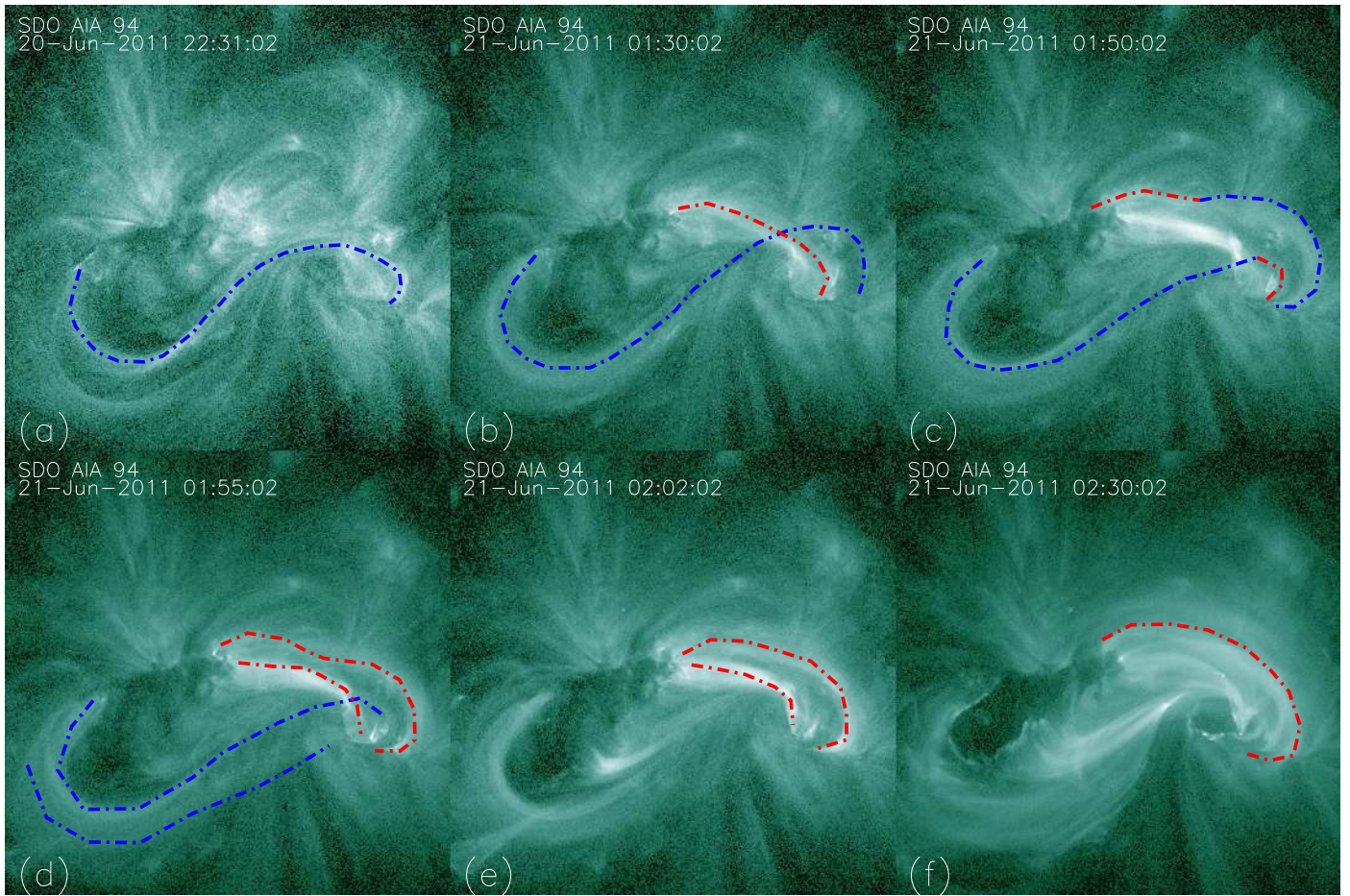


Figure 8. Morphological evolution of the eruption in the *SDO/AIA* 94 Å passband. Panel (a) gives a distinct sigmoid (outlined by the blue dotted–dashed line) 2.5 hr before the flare onset. During the precursor phase in panel (b), the overlying arcade (red dotted–dashed line) interacts with the western elbow of the sigmoid. Panels (c) and (d) show the deformation caused by the interaction and the exchanged lines during the reconnection between the overlying arcade and the western elbow. Panels (e) and (f) show the eruption of the sigmoid in its impulsive phase.

source regions of the two phases—precursor and impulsive phases are set at the flank (west elbow) and the main body of the sigmoid structure, respectively. Chifor et al. (2007) have disclosed the evidence of discrete, localized X-ray brightenings 2–50 minutes prior to the impulsive phase as the observable signatures of the preflare activity. The locations of these forerunners—transient preflare brightenings—were along the PILs, but not necessarily co-located with the source region of CMEs. Limited by observation instruments, the mechanism of the generation and interaction for the precursor phenomenon is only explained in a hypothetical model in their study. In the following, we present direct observational evidence of the source origin of the preflare brightening.

3.5. Morphological Evolution

All the observational results presented above point out that the event experienced a two-phase evolution during the eruption: a precursor phase and an impulsive phase. Here we further look into the morphological evolution starting even before the precursor phase. A clear view of the full evolution of the sigmoid in this active region was detected in high-temperature passbands of *SDO/AIA* face-on observations. From the long evolution of the active region in Figure 8, it shows that, 3 hr before the event onset, or at ~22:31 UT on 2011 June 20, the high-temperature sigmoidal structure had

appeared already with a bundle of arcade fields surrounding its western elbow. During the early time of the precursor phase, the arcade brightened around the western elbow of the sigmoid. However, no obvious movement or deformation of the structure was noticeable during this period. As time elapses, the western elbow of the sigmoid appeared smaller, and a concave-shaped loop arcade appeared just beside the western elbow of the sigmoid (Figures 8(c), (d)). As mentioned earlier, there was also a hard X-ray source at the western elbow (attached movie) during this period. The location of the X-ray source region did not change, as the western elbow was undergoing the morphological transformation due to the reconnection. From 01:50 UT to 02:00 UT, the arcade around the western elbow of the MFR began to light up and the topological configuration deformed from the loop shape to the concave shape and finally became a loop shape again, but at a larger size and an outer location. All these morphological evolutions could clearly be seen in the hot passbands, e.g., 94 Å ($T \sim 6.3$ MK), and 131 Å ($T \sim 10$ MK). Contrary to the dynamic changes shown in high temperatures, the low-temperature passbands such as the 304 Å ($T \sim 0.05$ MK) and 171 Å ($T \sim 0.63$ MK) only showed the flow motion of the prominence instead of the hot sigmoid and overlying arcades. The period of obvious morphological change at the western elbow (01:50 UT to 02:20 UT) coincided well with the weak acceleration of the sigmoid from 20 to 50 km s⁻¹ (Figure 5(d)).

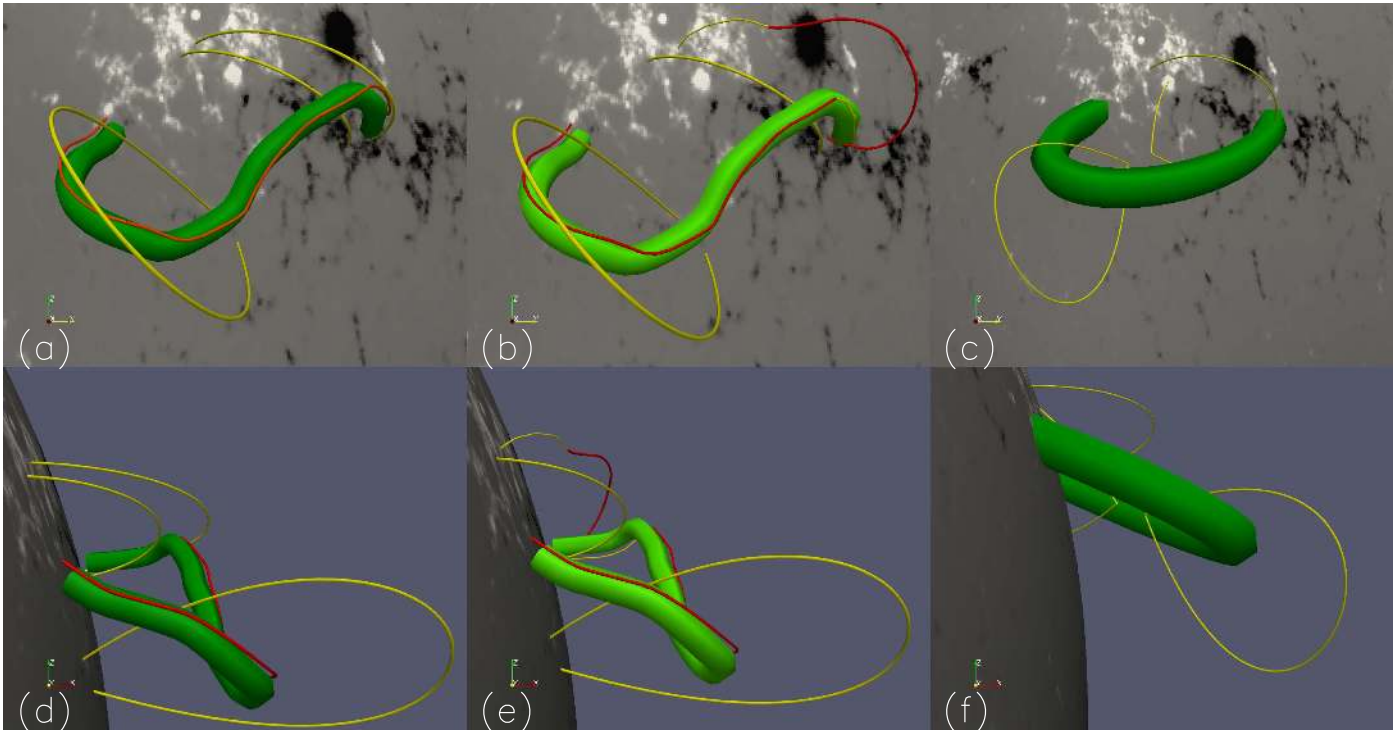


Figure 9. Schematic 3D model of the eruption, showing the flux rope (dark green tube), a representative field line (red) tracing the flux rope, and the ambient overlying arcade (yellow) around the western elbow arm/shoulder part of the sigmoid. The top row is the front view, and the bottom row is the axial view. The pre-eruption stage is shown in panels (a) and (d). The precursor phase is shown in panels (b) and (e): the interaction happens between the overlying arcade and the western elbow of the flux rope, and the field lines exchange during the reconnection. The impulsive phase is shown in panels (c) and (f): the flare reconnection triggers the fast eruption of the flux rope.

After 02:20 UT, the X-ray source regions were mainly located at the main body of the sigmoid, likely due to the main flare reconnection.

4. Summary and Discussion

In this paper, we have analyzed an extremely LDE. Using the tie-pointing method (Thompson 2009), we successfully reconstructed the true 3D structure of the MFR. Its overall topology in 3D can be described as an “m” shape. Due to the projection effect, the eastern and western elbows, suspended high on either side of the PIL, are projected on the disk as the hooks of the sigmoid from the face-on view of *SDO*, but more like a highly kinked “8” shape viewed along the axis from the side view of *STEREO*. The time evolution of the event, as observed in morphology, kinematics, and X-ray spectrum, indicates that the eruption process is not a single monotonic one. The eruption of this extremely long duration event has two distinct phases: a precursor phase and an impulsive or main phase. Any viable theoretical model shall explain the onset mechanism and the physical driver of the two phases, as constrained by rich observations provided in this event.

We interpret the hot sigmoidal structure and the near co-spatial filament as a magnetic configuration of an MFR. We further explain the observations using the cartoon model in Figure 9 based on the preexistence of an MFR. The MFR is intrinsically unstable owing to its own Lorentz self-force or hoop force. The existence of a stable MFR is achieved through the presence of the overlying magnetic field, which exerts a downward strapping force onto the MFR. We believe that, prior to the onset of the precursor phase ($\sim 01:30$ UT), the MFR is well in the balance between the hoop force and the strapping

force. Based on the observations gathered for this event, we tend to assume that the onset of the precursor phase is triggered by the torus instability of the MFR. The torus instability likely drives the magnetic reconnection between the magnetic field line of the overlying arcade and the field line wrapping around the outer layer of the MFR. The effect of this reconnection is to peel off the overlying field, thus reducing the strapping effect and allowing the MFR to rise up. The reason why we do not think that this reconnection occurred under the MFR is listed as follows. From Figure 8(b), the newly brightened loop systems had a cross point near the western elbow of the MFR from the top view. As the reconnection went on, the newly formed loops concaved down and finally became a semicircular shape. If the reconnection had occurred below, the configuration would have required the entire western leg of the MFR to be cut off by the reconnection, which was not observed. Such reconnection above the eruption structure during the precursor phase is called external reconnection (Sterling & Moore 2005). In their study, the core field (or flux rope in our interpretation) was under a slow rising motion, and reconnection occurred above the core field lit up the side lobe region. This slow but persistent rising motion eventually led to the onset of the impulsive phase or the main phase. While we observe that the onset of the impulsive phase was a consequence of the rising motion of the flux rope, it is not entirely clear what physical mechanism triggered the onset. One possibility is that it was triggered by the fast flare reconnection underneath the eruption structure, as suggested by the classical eruptive flare model (CSHKP model; Carmichael 1964; Sturrock 1966; Hirayama 1974; Kopp & Pneuman 1976). In this scenario, the reconnection occurs in the vertical current sheet formed by the stretching of the surrounding magnetic field of the MFR.


The reconnection serves as the role of tether cutting, thus quickly removing the strapping force of the overlying field and allowing the strong and impulsive acceleration of the MFR. In this scenario, the onset of the precursor phase is caused by the torus instability, and the onset of the impulsive phase is caused by the fast magnetic reconnection within the vertical current sheet underneath the MFR.

The AIA data used here are courtesy of *SDO* (NASA) and the AIA consortium. We thank the AIA team for the easy access to calibrated data. The SECCHI data are courtesy of *STEREO* and the SECCHI consortium. *RHESSI* is a NASA Small Explorer. *Hinode* is a Japanese mission developed and launched by ISAS/JAXA. We are grateful to the *SDO*, *STEREO*, *HESSI*, and *Hinode* consortium for the free access to the data. Z.Z. and Y.W. are supported by NSFC (41574165, 41421063) and CAS (Key Research Program of Frontier Sciences QYZDB-SSW-DQC015, KZZD-EW-01-4). Z.Z. is also supported by the scholarship granted by the China Scholarship Council (CSC) under file no. 201406340073. J.Z. is supported by NSF grants AGS-1249270 and AGS-1460188. G.C. acknowledges support by the NASA Earth and Space Science Fellowship Program grant NNX12AL73H.

ORCID iDs

Zhenjun Zhou (周振军)  <https://orcid.org/0000-0001-7276-3208>

Jie Zhang  <https://orcid.org/0000-0003-0951-2486>

Yuming Wang  <https://orcid.org/0000-0002-8887-3919>

Rui Liu  <https://orcid.org/0000-0003-4618-4979>

Georgios Chintzoglou  <https://orcid.org/0000-0002-1253-8882>

References

- Antiochos, S. K., DeVore, C. R., & Klimchuk, J. A. 1999, *ApJ*, **510**, 485
- Aurass, H., Vourlidas, A., Andrews, M. D., et al. 1999, *ApJ*, **511**, 451
- Benz, A. O. 1993, *Plasma Astrophysics: Kinetic Processes in Solar and Stellar Coronae* (Vol. 184; Dordrecht: Kluwer)
- Boerner, P., Edwards, C., Lemen, J., et al. 2012, *SoPh*, **275**, 41
- Bumba, V., & Křivský, L. 1959, *BAICz*, **10**, 221
- Burlaga, L., Sittler, E., Mariani, F., & Schwenn, R. 1981, *JGR*, **86**, 6673
- Burlaga, L. F. 1995, in *Interplanetary Magnetohydrodynamics*, ed. L. F. Burlaga (Oxford: Oxford Univ. Press), 272
- Canfield, R. C., Hudson, H. S., & McKenzie, D. E. 1999, *GeoRL*, **26**, 627
- Canfield, R. C., Kazachenko, M. D., Acton, L. W., et al. 2007, *ApJL*, **671**, L81
- Canou, A., Amari, T., Bommier, V., et al. 2009, *ApJL*, **693**, L27
- Carmichael, H. 1964, *NASSP*, **50**, 451
- Chae, J., Wang, H., Qiu, J., et al. 2001, *ApJ*, **560**, 476
- Cheng, C.-C., Pallavicini, R., Acton, L. W., & Tandberg-Hanssen, E. 1985, *ApJ*, **298**, 887
- Cheng, X., Ding, M. D., Guo, Y., et al. 2010, *ApJL*, **716**, L68
- Cheng, X., Ding, M. D., Guo, Y., Zhang, J., et al. 2014a, *ApJ*, **780**, 28
- Cheng, X., Ding, M. D., Zhang, J., et al. 2014b, *ApJL*, **789**, L35
- Cheng, X., Zhang, J., Liu, Y., & Ding, M. D. 2011, *ApJL*, **732**, L25
- Cheng, X., Zhang, J., Saar, S. H., & Ding, M. D. 2012, *ApJ*, **761**, 62
- Chifor, C., Tripathi, D., Mason, H. E., & Dennis, B. R. 2007, *A&A*, **472**, 967
- Chintzoglou, G., Patsourakos, S., & Vourlidas, A. 2015, *ApJ*, **809**, 34
- Contarino, L., Romano, P., Yurchyshyn, V. B., & Zuccarello, F. 2003, *SoPh*, **216**, 173
- Fárník, F., Hudson, H. S., Karlický, M., & Kosugi, T. 2003, *A&A*, **399**, 1159
- Gibson, S. E., & Fan, Y. 2006, *JGRA*, **111**, A12103
- Golub, L., Deluca, E., Austin, G., et al. 2007, *SoPh*, **243**, 63
- Golub, L., Deluca, E. E., Sette, A., & Weber, M. 2004, in *ASP Conf. Ser. 325, The Solar-B Mission and the Forefront of Solar Physics*, ed. T. Sakurai & T. Sekii, 217
- Gosling, J. T. 1990, *GMS*, **58**, 343
- Green, L. M., & Kliem, B. 2009, *ApJL*, **700**, L83
- Green, L. M., Kliem, B., & Wallace, A. J. 2010, *A&A*, **526**, A2
- Guo, Y., Schmieder, B., Démoulin, P., et al. 2010, *ApJ*, **714**, 343
- Hannah, I. G., & Kontar, E. P. 2012, *A&A*, **539**, A146
- Hirayama, T. 1974, *SoPh*, **34**, 323
- Hood, A. W., & Priest, E. R. 1981, *GApFD*, **17**, 297
- Howard, R. A., Moses, J. D., Vourlidas, A., et al. 2008, *SSRv*, **136**, 67
- Huang, J., Démoulin, P., Pick, M., et al. 2011, *ApJ*, **729**, 107
- Illing, R. M. E., & Hundhausen, A. J. 1985, *JGR*, **90**, 275
- Kliem, B., & Török, T. 2006, *PhRvL*, **96**, 255002
- Kopp, R. A., & Pneuman, G. W. 1976, *SoPh*, **50**, 85
- Kosugi, T., Matsuzaki, K., Sakao, T., et al. 2007, *SoPh*, **243**, 3
- Kumar, A., & Rust, D. M. 1996, *JGR*, **101**, 15667
- Lemen, J. R., Title, A. M., Akin, D. J., et al. 2012, *SoPh*, **275**, 17
- Lepping, R. P., Burlaga, L. F., & Jones, J. A. 1990, *JGR*, **95**, 11957
- Lin, R. P., Dennis, B. R., Hurford, G. J., et al. 2002, *SoPh*, **210**, 3
- Liu, L., Wang, Y., Wang, J., et al. 2016, *ApJ*, **826**, 119
- Liu, R., Kliem, B., Titov, V. S., et al. 2016, *ApJ*, **818**, 148
- Liu, R., Liu, C., Wang, S., Deng, N., & Wang, H. 2010, *ApJL*, **725**, L84
- Martin, S. F. 1980, *SoPh*, **68**, 217
- Moore, R. L., & Sterling, A. C. 2006, *GMS*, **165**, 43
- Moore, R. L., Sterling, A. C., Hudson, H. S., & Lemen, J. R. 2001, *ApJ*, **552**, 833
- Narukage, N., Sakao, T., Kano, R., et al. 2011, *SoPh*, **269**, 169
- O'Dwyer, B., Del Zanna, G., Mason, H. E., Weber, M. A., & Tripathi, D. 2010, *A&A*, **521**, A21
- Olmedo, O., & Zhang, J. 2010, *ApJ*, **718**, 433
- Patsourakos, S., Vourlidas, A., & Stenborg, G. 2013, *ApJ*, **764**, 125
- Pesnell, W. D., Thompson, B. J., & Chamberlin, P. C. 2012, *SoPh*, **275**, 3
- Pevtsov, A. A. 2002, in *COSPAR Colloq. Ser. 13, Multiwavelength Observations of Coronal Structure and Dynamics*, ed. P. Martens & D. Cauffman (Dordrecht: Pergamon), 125
- Pevtsov, A. A., Canfield, R. C., & Zirin, H. 1996, *ApJ*, **473**, 533
- Qiu, J., Hu, Q., Howard, T. A., & Yurchyshyn, V. B. 2007, *ApJ*, **659**, 758
- Riley, P., Lionello, R., Mikić, Z., & Linker, J. 2008, *ApJ*, **672**, 1221
- Rust, D. M., & Kumar, A. 1994, *SoPh*, **155**, 69
- Rust, D. M., & Kumar, A. 1996, *ApJL*, **464**, L199
- Savcheva, A. S., McKillop, S. C., McCauley, P. I., Hanson, E. M., & DeLuca, E. E. 2014, *SoPh*, **289**, 3297
- Schmelz, J. T., Worley, B. T., Anderson, D. J., et al. 2011, *ApJ*, **739**, 33
- Schrijver, C. J., Elmore, C., Kliem, B., Török, T., & Title, A. M. 2008, *ApJ*, **674**, 586
- Song, H. Q., Zhang, J., Cheng, X., et al. 2014, *ApJ*, **784**, 48
- Sterling, A. C., & Moore, R. L. 2005, *ApJ*, **630**, 1148
- Sturrock, P. A. 1966, *Natur*, **211**, 695
- Su, Y., & van Ballegooyen, A. 2012, *ApJ*, **757**, 168
- Tandberg-Hanssen, E. 2013, *The Nature of Solar Prominences* (Vol. 199; Dordrecht: Kluwer)
- Thompson, W. T. 2009, *Icar*, **200**, 351
- Titov, V. S., & Démoulin, P. 1999, *A&A*, **351**, 707
- Török, T., Kliem, B., & Titov, V. S. 2004, *A&A*, **413**, L27
- Tripathi, D., Kliem, B., Mason, H. E., Young, P. R., & Green, L. M. 2009, *ApJL*, **698**, L27
- van Hoven, G., & Hurford, G. J. 1984, *AdSpR*, **4**, 95
- Vourlidas, A., Lynch, B. J., Howard, R. A., & Li, Y. 2013, *SoPh*, **284**, 179
- Vršnak, B., Brajša, R., Wöhl, H., et al. 2003, *A&A*, **404**, 1117
- Wang, Y., Zhou, Z., Shen, C., Liu, R., & Wang, S. 2015, *JGRA*, **120**, 1543
- Wang, Y., Zhuang, B., Hu, Q., et al. 2016, *JGRA*, **121**, 9316
- Warren, H. P., & Warshall, A. D. 2001, *ApJL*, **560**, L87
- Weber, M. A., Deluca, E. E., Golub, L., & Sette, A. L. 2004, in *IAU Symp. 223, Multi-Wavelength Investigations of Solar Activity*, ed. A. V. Stepanov, E. E. Benevolenskaya, & A. G. Kosovichev (Cambridge: Cambridge Univ. Press), 321
- Wiegelmann, T., & Sakurai, T. 2012, *LRSP*, **9**, 5
- Williams, D. R., Török, T., Démoulin, P., van Driel-Gesztelyi, L., & Kliem, B. 2005, *ApJL*, **628**, L163
- Wuclser, J.-P., Lemen, J. R., Tarbell, T. D., et al. 2004, *Proc. SPIE*, **5171**, 111
- Zhang, J., Cheng, X., & Ding, M.-D. 2012, *NatCo*, **3**, 747
- Zhang, J., & Dere, K. P. 2006, *ApJ*, **649**, 1100
- Zhang, J., Dere, K. P., Howard, R. A., Kundu, M. R., & White, S. M. 2001, *ApJ*, **559**, 452
- Zhou, G. P., Zhang, J., & Wang, J. X. 2016, *ApJL*, **823**, L19